arXiv:1007.4194v1 [astro-ph.CO] 23 Jul 2010

WARM MOLECULAR HYDROGEN EMISSION IN NORMAL EDGE-ON GALAXIES NGC 4565 AND NGC 5907

Seppo Laine

Spitzer Science Center - Caltech, MS 220-6, Pasadena, CA 91125; seppo@ipac.caltech.edu

Philip N. Appleton

NASA Herschel Science Center, California Institute of Technology, Pasadena, CA 91125, USA; apple@ipac.caltech.edu

Stephen T. Gottesman

Department of Astronomy, University of Florida, Gainesville, FL 32611-2055; gott@astro.ufl.edu

Matthew L. N. Ashby

Harvard-Smithsonian Center for Astrophysics, 60 Garden Street, Cambridge, MA 02138; mashby@cfa.harvard.edu

AND

Catherine A. Garland

Natural Sciences Department, Castleton State College, Castleton, VT 05735; catherine.garland@castleton.edu

To appear in AJ

ABSTRACT

We have observed warm molecular hydrogen in two nearby edge-on disk galaxies, NGC 4565 and NGC 5907, using the *Spitzer* high-resolution infrared spectrograph. The 0–0 S(0) 28.2 μm and 0–0 S(1) 17.0 μm pure rotational lines were detected out to 10 kpc from the center of each galaxy on both sides of the major axis, and in NGC 4565 the S(0) line was detected at $r = 15$ kpc on one side. This location is beyond the transition zone where diffuse neutral atomic hydrogen starts to dominate over cold molecular gas, and marks a transition from a disk dominated by high surface-brightness far-IR emission to that of a more quiescent disk. It also lies beyond a steep drop in the radio continuum emission from cosmic rays in the disk. Despite indications that star formation activity decreases with radius, the H_2 excitation temperature and the ratio of the H_2 line and the far-IR luminosity surface densities, $\Sigma(L_{H2})/\Sigma(L_{TIR})$, change very little as a function of radius, even into the diffuse outer region of the disk of NGC 4565. This suggests that the source of excitation of the H_2 operates over a large range of radii, and is broadly independent of the strength and relative location of UV emission from young stars. Although excitation in photodissociation regions is the most common explanation for the widespread H_2 emission, cosmic ray heating or shocks cannot be ruled out. At $r = 15$ kpc in NGC 4565, outside the main UV and radio continuum-dominated disk, we derived a higher than normal H_2 to 7.7 μm PAH emission ratio, but this is likely due to a transition from mainly ionized PAH molecules in the inner disk to mainly neutral PAH molecules in the outer disk. The inferred mass surface densities of warm molecular hydrogen in both edge-on galaxies differ substantially, being 4(–60) $M_\odot$ pc^{-2} and 3(–50) $M_\odot$ pc^{-2} at $r = 10$ kpc for NGC 4565 and NGC 5907, respectively. The higher values represent very unlikely point-source upper limits. The point source case is not supported by the observed emission distribution in the spectral slits. These mass surface densities cannot support the observed rotation velocities in excess of 200 km s^{-1}. Therefore, warm molecular hydrogen cannot account for dark matter in these disk galaxies, contrary to what was implied by a previous *ISO* study of the nearby edge-on galaxy NGC 891.

Subject headings: galaxies: structure — galaxies: ISM — galaxies: evolution — galaxies: individual (NGC 4565, NGC 5907)

1. INTRODUCTION

The physical conditions and excitation mechanisms of atomic and molecular gas in the outer disks of nearby spiral galaxies are only beginning to be explored. Most of this gas is thought to be neutral atomic hydrogen (H I), or cold (T < 50 K) molecular hydrogen (H_2). The presence of cold H_2 is usually inferred only by indirect means via observations of carbon monoxide (CO), and quantified by assuming an (uncertain) empirical conversion factor between the two molecules. Direct detection of H_2 is preferable. However, since H_2 has no allowed dipole radiative transitions, it has to be heated above ~ 100 K to radiate significantly via quadrupole pure-rotational transitions in the mid-infrared (mid-IR) or through rovibrational transitions from even warmer gas emerging in the near-infrared. Furthermore, the other direct observational window – the detection through the absorption of UV radiation in the electronic Lyman–Werner bands – is challenging, and only under rare conditions has it been possible to detect the presence of cold H_2 in the Galaxy through FUV absorption (e.g., Snow et al. 2000;
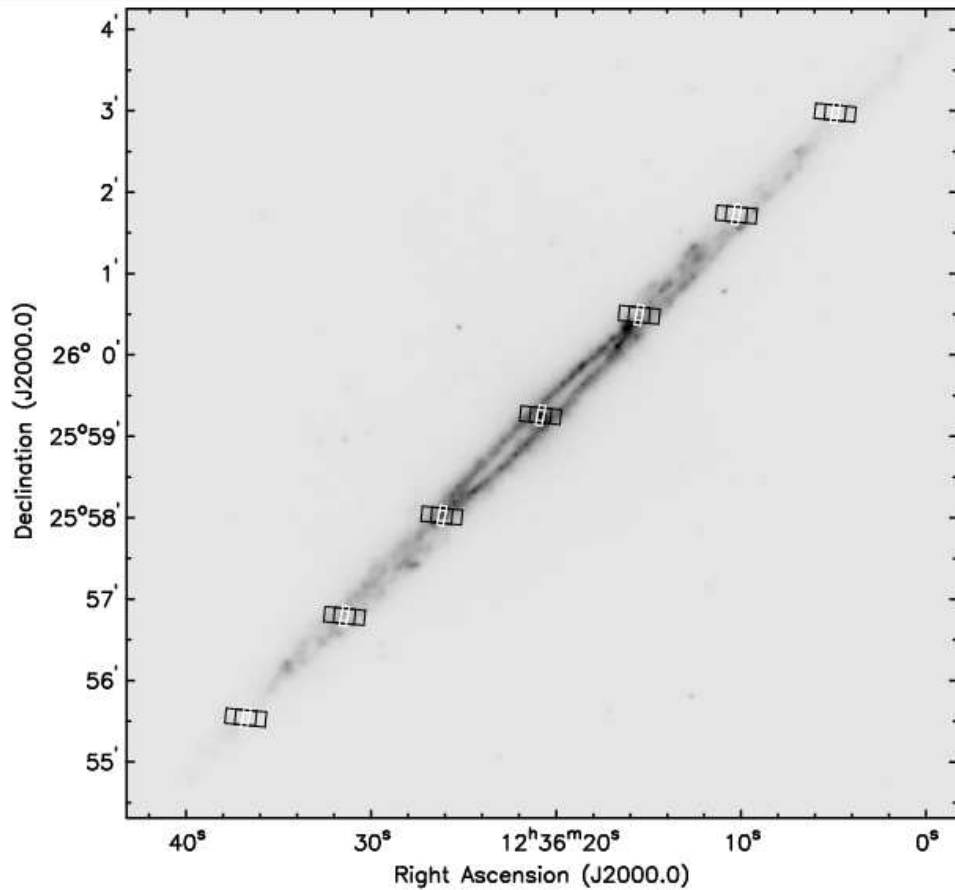
Figure 1. Positions of the IRS SH (white) and LH (black) slits overlaid on an 8 μm *Spitzer*/IRAC image of NGC 4565. Spectra from $\sim$ 10 to 37 μm were taken at the nucleus and at distances of 5, 10, and 15 kpc from the nucleus along the galaxy's major axis. Emission from warm H_2 was detected even at the farthest northwestern (top right) position.
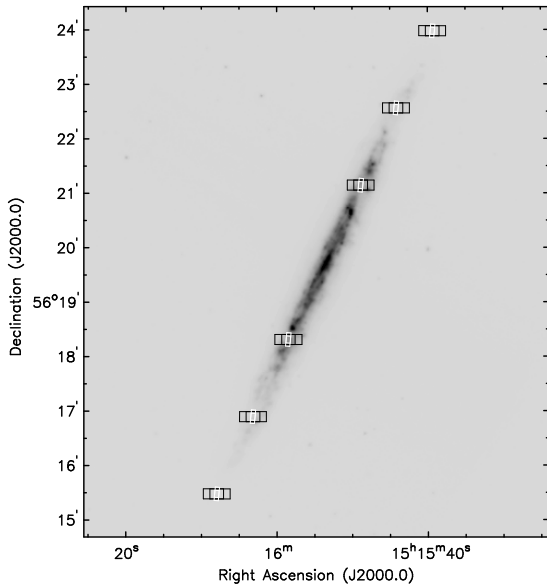

Figure 2. Positions of the IRS SH (white) and LH (black) slits overlaid on an 8 μm *Spitzer*/IRAC image of NGC 5907. Spectra from $\sim$ 10 to 37 μm were taken at the nucleus and at distances of 5, 10, and 15 kpc from the nucleus along the galaxy's major axis.

Rachford et al. 2009).

The *Infrared Space Observatory (ISO)* provided the first opportunity to directly observe warm extragalac-tic molecular hydrogen in nearby galaxies, unham-pered by the atmosphere (e.g., Rigopoulou et al. 1996; Valentijn et al. 1996; Valentijn & van der Werf 1999). More recently the *Spitzer Space Telescope* (Werner et al. 2004) has provided a wealth of new data on rota-tional H_2 emission lines in dozens of nearby galaxies, ranging from normal galaxies (e.g., Roussel et al. 2007; Brunner et al. 2008) to Ultraluminous Infrared Galax-ies (ULIRGs; Armus et al. 2006). Unusually strong intergroup H_2 emission associated with a large-scale ($\sim$ 30 kpc) X-ray emitting shock has recently been found associated with the compact Stephan's Quintet galaxy group (Appleton et al. 2006; Cluver et al. 2010) and the *Taffy Galaxy* bridge (B. W. Peterson et al. 2010, in preparation). Similarly large H_2 line fluxes have been found in 17 galaxies in a sample of 55 low-luminosity radio galaxies (Ogle et al. 2007; Ogle et al. 2010). In Stephan's Quintet and in the low-luminosity radio galax-ies, very weak thermal continua are detected, suggesting shock excitation of H_2, rather than excitation via pho-todissociation regions (PDRs) associated with star for-mation (e.g., Guillard et al. 2009). Other sources of H_2 heating, for example cosmic ray heating, have also been suggested to explain the strong H_2 emission in the Orion bar (Shaw et al. 2009).

It is therefore of interest to examine the strength of H_2 emission in the outer regions of nearby galaxies, where star formation and cosmic ray heating are much reduced,
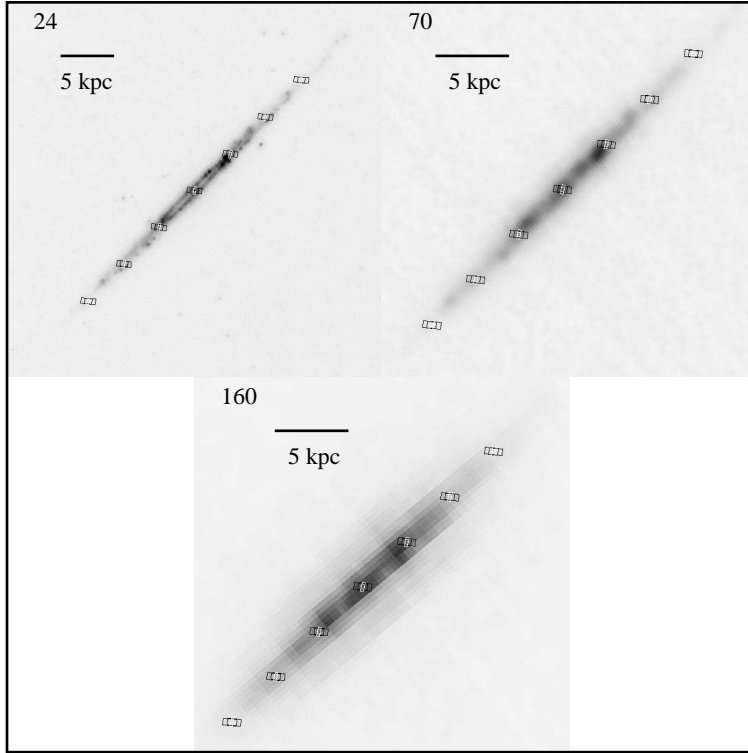
Figure 3. Archival *Spitzer*/MIPS images of NGC 4565 at 24 μm (upper left), 70 μm (upper right), and 160 μm (bottom). The SH (white) and LH (black) slit positions have been overlaid.

and where the dominant gas component is usually assumed to be neutral atomic hydrogen rather than molecular gas. By outer regions in this paper we mean the radii 10 kpc and beyond from the nucleus. *ISO* observations of the nearby edge-on galaxy NGC 891 directly detected the abundant warm H_2 out to a distance of 11 kpc from the galaxy center (Valentijn & van der Werf 1999), with warm H_2 mass surface densities of $\sim 3000 \, M_\odot \, pc^{-2}$. This suggested a dominant contribution of molecular hydrogen to the mass-density of the disk, and perhaps that molecular hydrogen could contribute a significant part of the "missing mass" in this galaxy.

Intrigued by these early *ISO* results, we pursued *Spitzer* Infrared Spectrograph (IRS; Houck et al. 2004) observations of two local, nearly edge-on galaxies, NGC 4565 and NGC 5907, to explore the possibility of massive reservoirs of warm molecular gas far from the nuclei. These early-mission IRS high resolution spectra cover infrared wavelengths from 10 μm to 37 μm, and target the 0–0 S(0) and 0–0 S(1) H_2 lines, which are known to contain the strongest emission from the mass in warm molecular gas in nearby galaxies (e.g., Roussel et al. 2007). The spectral range also covered several other mid-IR lines which assisted us in exploring the importance of star formation as an excitation mechanism in these regions. Although the current observations are not extremely sensitive, they provide interesting constraints on the nature of H_2 emission in the outer disks of galaxies.

To assist in our analysis, we also utilized *Spitzer* Infrared Array Camera (IRAC) 8 μm images of NGC 4565 (Figure 1) and NGC 5907 (Figure 2) taken in *Spitzer* program PID 3 (P.I. Giovanni Fazio; M. L. N. Ashby 2009, private communication). Finally, we utilized archival

Spitzer Multiband Imaging Photometer (MIPS) images of NGC 4565 and NGC 5907 at 24, 70, and 160 μm (Figure 3 shows these maps for NGC 4565).

NGC 4565 is a nearby (we adopted a distance of 10 Mpc for our observations), Sb-type nearly edge-on (inclination 88°; Alton et al. 2004) large (D$_{25}$=15′.8) disk galaxy with a nucleus classified as Sy1.9 (Deo et al. 2007). A sharp dust lane delineates the disk plane of the galaxy, and there is significant obscuration caused by dust within the galactic plane. Neininger et al. (1996) found that this galaxy has a nuclear molecular disk as well as a molecular gas ring at a distance of $\sim 1'$–$2'$ (3–6 kpc) from the nucleus, and weaker extended molecular gas emission. The molecular gas ring has an associated dust ring, which is seen in the *Spitzer* 8 μm image shown in Figure 1. The H I distribution is asymmetric along the disk plane, with substantially more emission coming from the northwestern side, and there is a strong, continuous warp in the H I emission starting at $\sim 7'$ on both sides of the nucleus (Rupen 1991). Sofue & Nakai (1994) showed that at a radius of ~ 10 kpc the interstellar medium (ISM) transitions from being dominated by molecular gas to being dominated by atomic gas.

NGC 5907 is a similarly large (D$_{25}$=12′.6), nearby (adopted distance 11 Mpc), almost edge-on (inclination 87°; Alton et al. 2004), disk galaxy. CO observations show a fast-rotating nuclear molecular disk with bar-like non-circular motions beyond the nucleus (García–Burillo, Guélin, & Neininger 1997). The H I distribution shows a warp at both the southeastern and northwestern sides of the nucleus, starting at $\sim 5'$ radius (Sancisi 1976; Shang et al. 1998).
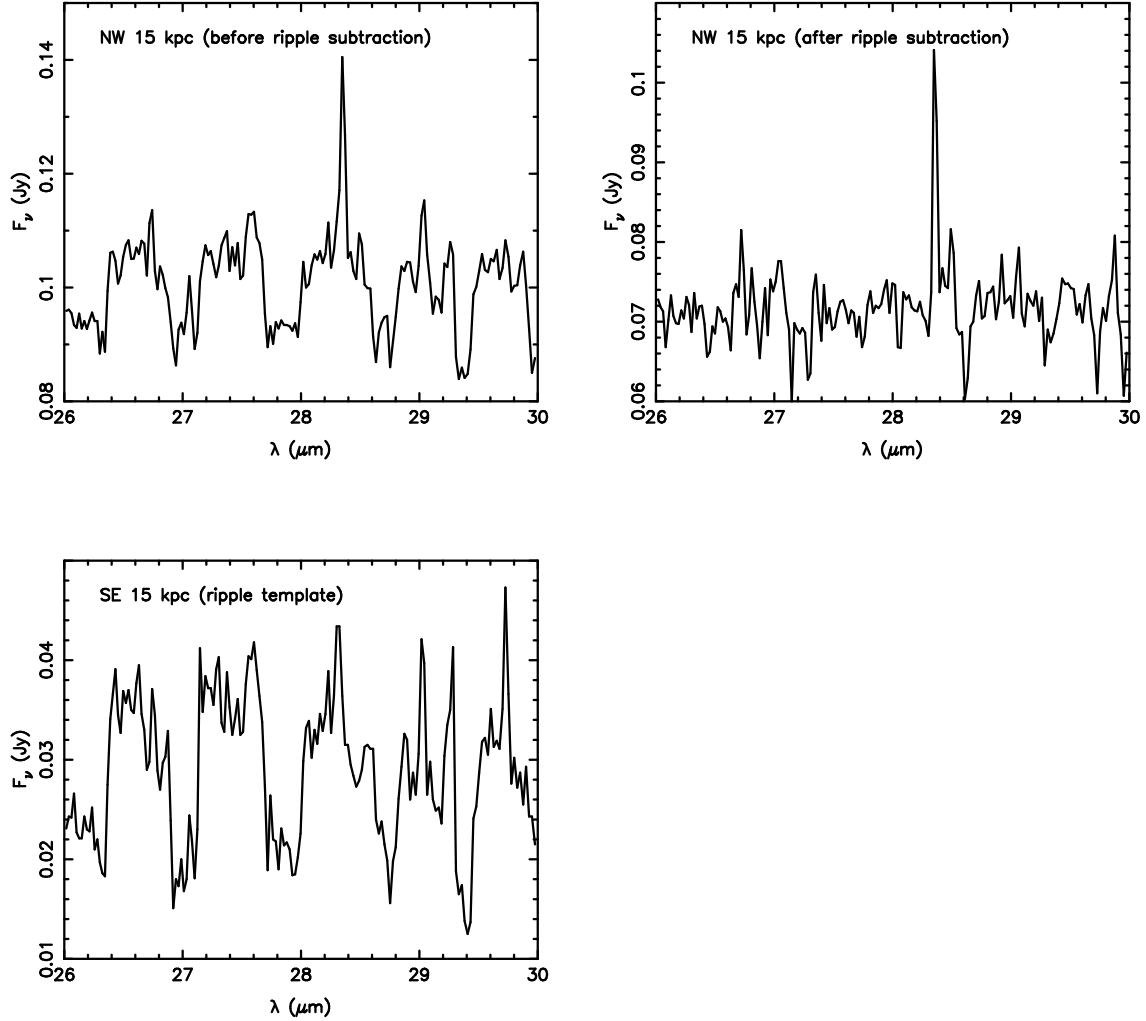
2. OBSERVATIONS

Figure 4. Ripple spectrum subtraction. The original spectrum around the 28 micron H_2 line in NGC 4565 at 15 kpc NW is at top left, the same spectrum after the "ripple spectrum" subtraction is at top right, and the "ripple spectrum" from the SE 15 kpc position is at bottom left.

Table 1
Forbidden lines in NGC 4565.

Position	[NeII]12.81μm[a]	[NeIII]15.55μm[a]	[SIII]18.71μm[a]	[SIII]33.48μm[b]	[SiII]34.81μm[b]
SE 5 kpc Ex	187±6	44±5	65±6	335±13	397±15
SE 5 kpc Pt	283±9	73±9	118±10	531±21	650±15
SE 10 kpc Ex	95±5	28±12	48±4	284±6	234±13
SE 10 kpc Pt	144±7	47±20	88±8	386±9	383±13
SE 15 kpc Ex	30±7	< 14	13±3	⋯	⋯
SE 15 kpc Pt	45±11	< 23	24±5	⋯	⋯
NW 5 kpc Ex	207±6	40±5	87±3	411±8	487±7
NW 5 kpc Pt	314±9	67±9	158±6	652±13	799±11
NW 10 kpc Ex	69±3	41±5	36±3	199±6	144±5
NW 10 kpc Pt	104±5	68±7	65±5	316±10	236±8
NW 15 kpc Ex	28±8	28±8	< 10	40±5	69±8
NW 15 kpc Pt	43±12	47±13	< 19	64±8	113±13

Note. — Measured line fluxes are given in 10^{-19} W m^{-2}.

We observed NGC 4565 and NGC 5907 with both high resolution modules of *Spitzer's* IRS instrument on 2005 January 10 and 2005 June 6, respectively (PID 3319; ADS/Sa.Spitzer#00010745344 and ADS/Sa.Spitzer#00010745088). The short-high (SH) module covers wavelengths from 9.9 to 19.6 μm and has a slit size of 4″7 × 11″3, while the long-high (LH) mod-ule brackets the 18.7 to 37.2 μm wavelength range with a slit size of 11″1 × 22″3. We took one cycle of "staring mode" observations with a 120 s ramp time with the SH module and a 240 s ramp time with the LH module. The effective integration times were approximately doubled to $\sim$ 240 s (SH) and $\sim$ 480 s (LH) because each cycle takes two spectra, moving the target to positions 1/3 and 2/3
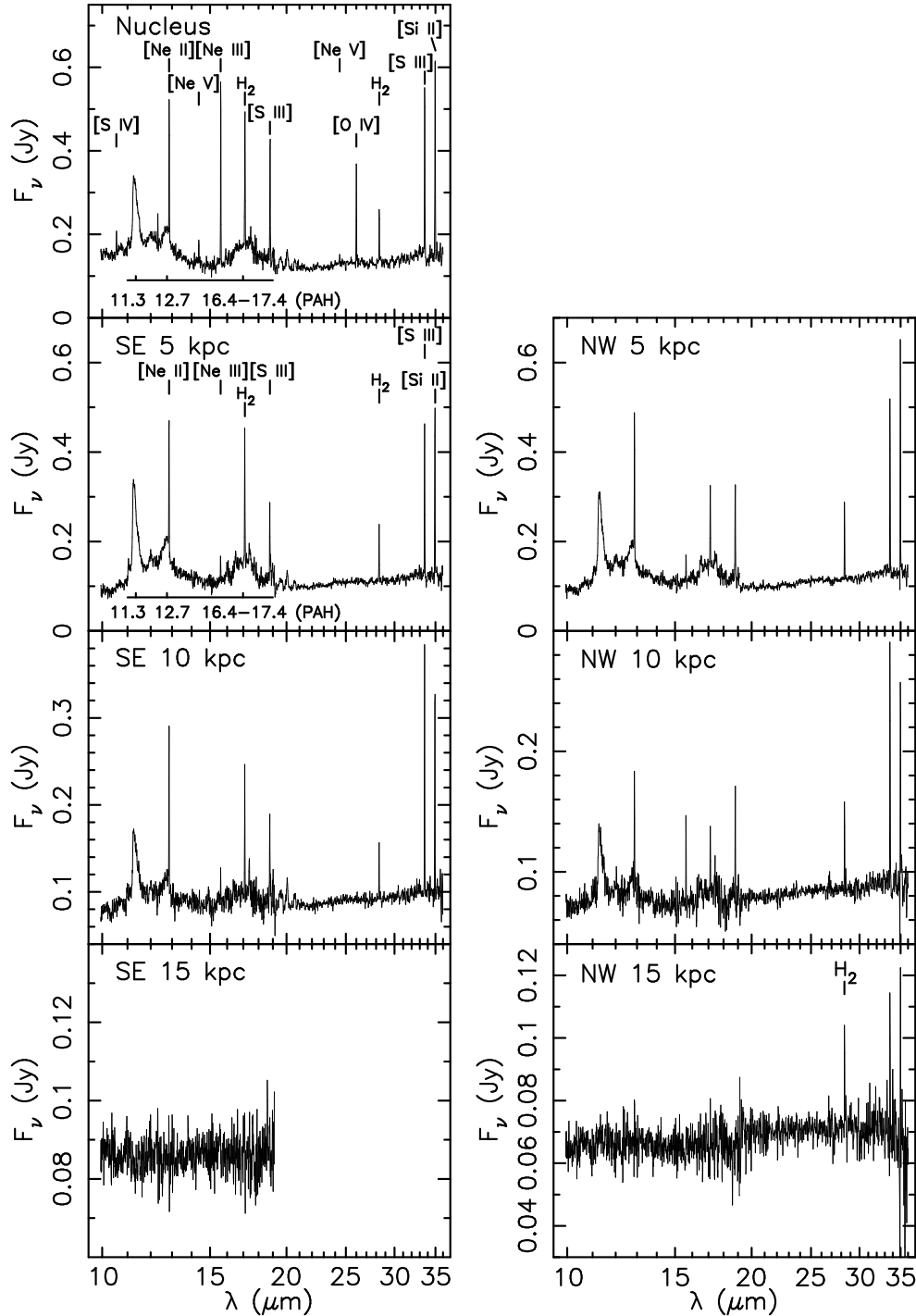
Figure 5. Combined SH and LH spectra of NGC 4565 at the seven positions shown in Figure 1. The observed flux density in Jy is plotted versus the observed wavelength in μm. H_2 is detected at all locations except the 15 kpc SE pointing. A variety of forbidden lines and broad PAH regions are also identified.

slit lengths away from the end of the slit along the slit long axis. We observed three positions along the galaxy major axes on both sides of the nuclei at distances of 5, 10, and 15 kpc from the nucleus. We also observed the nucleus of NGC 4565. Projections of the SH and LH slits on the 8 μm IRAC galaxy images are shown in Figures 1 and 2. By overlaying our observed positions on visible light and H I maps we confirmed that the gaseous and stellar warps start beyond the outermost observed locations in these two galaxies. Only in the northwest 15 kpc

pointing in NGC 5907 could a very small amount of H_2 have been missed if it strictly follows the H I distribution. However, even in that position the majority of H I emission comes from along the major axis of the galaxy.

The background brightnesses (due to ecliptic emission) were ~ 29 MJy sr^{-1} for NGC 4565, and 17–18 MJy sr^{-1} for NGC 5907. No separate background spectra were taken, since the recommended observing strategy during the first cycle of *Spitzer* observations was still evolving
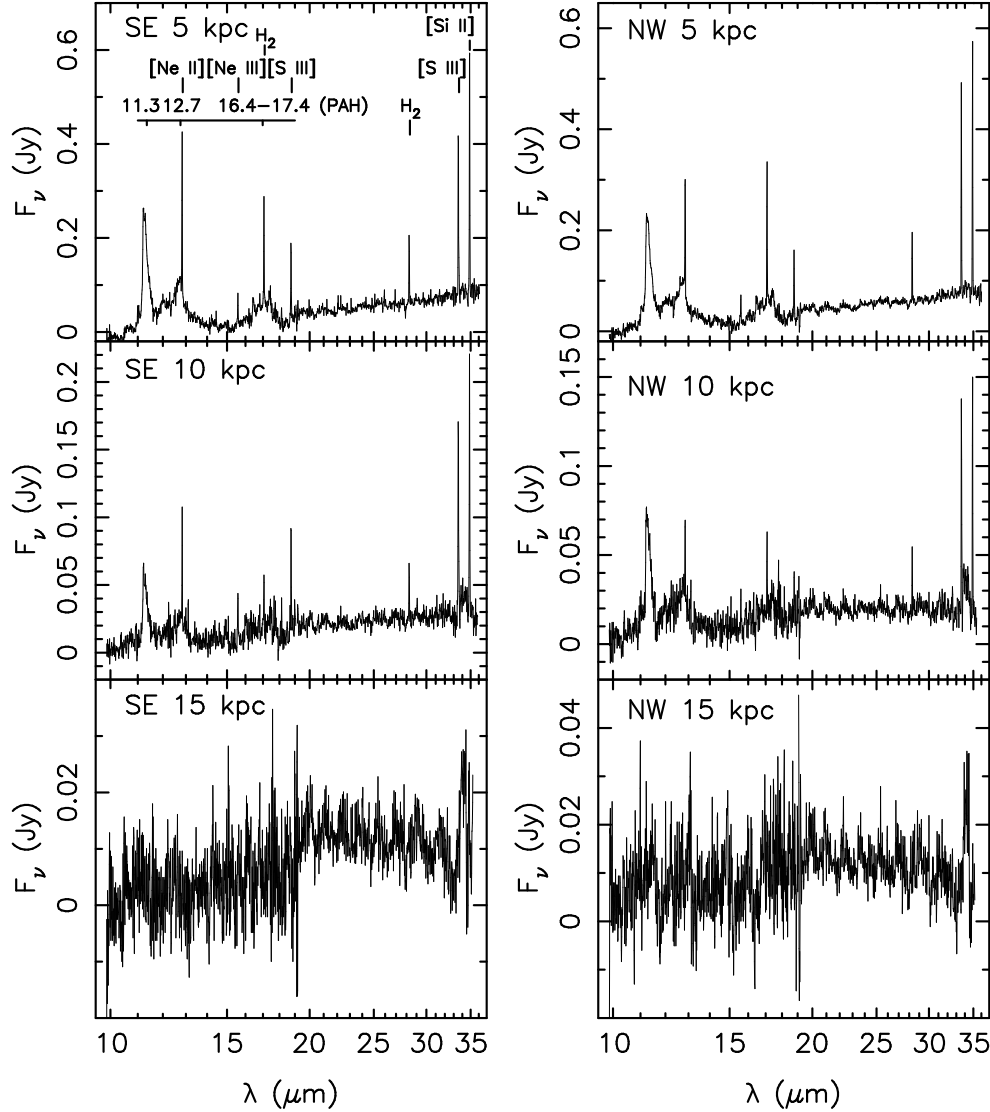
Figure 6. Combined SH and LH spectra of NGC 5907 at the six positions shown in Figure 2. The observed flux density in Jy is plotted versus the observed wavelength in μm. H_2 is detected at all but the two outermost pointings. A variety of forbidden lines and broad PAH regions are also identified.

Table 2
Forbidden lines in the nucleus of NGC 4565.

	SIV 10.51[a]	NeII 12.81[a]	NeV 14.32[a]	NeIII 15.55[a]	SIII 18.71[a]	NeV 24.31[b]	OIV 25.89[b]	SIII 33.48[b]	SiII 34.82[b]
Pt	55±9	322±6	47±3	354±8	238±13	52±7	431±11	726±13	867±21
Ex	39±6	213±4	30±2	212±5	131±7	37±5	302±8	457±8	529±13

Note. — Measured line fluxes are given in 10^{-19} W m^{-2}. The numbers after the ion species give the rest wavelength in microns.
[a] Integrated over the SH aperture (53 arcsec^2).
[b] Integrated over the LH aperture (248 arcsec^2).

and no clear recommendations existed at the time. This considerably complicated the removal of bad pixels from the spectra, discussed below. We did not use the "peak-up" option since our targets are extended, but the intrinsic IRS pointing accuracy of $\sim 1''$ was sufficient for our purposes.

We used spectra that were processed through the standard *Spitzer* IRS pipeline (version S13.2.0). We first edited the basic calibrated data frames to remove bad or "rogue" pixels, using a custom-made software script that allows interactive removal of isolated bad pixels from these data. We then ran the spectra through the S17 version of the custom spectral extraction software SPICE provided by the *Spitzer* Science Center, using the whole slit width extractions and initially the standard point source calibration for flux calibration.

Corrections were later made to line fluxes for both point and extended source calibration using the slit-loss

Table 3
H_2 line fluxes in NGC 4565.

Position	0–0 S(0)[b]	0–0 S(1)[a]	0–0 S(2)[a]
Nucleus Ex	189±5	170±7	29±6
Nucleus Pt	281±8	298±14	43±10
SE 5 kpc Ex	176±3	121±4	< 12
SE 5 kpc Pt	261±5	213±7	< 17
SE 10 kpc Ex	88±1	52 ±2	< 17
SE 10 kpc Pt	130±2	92±4	< 25
SE 15 kpc Ex	⋯	< 14	< 16
SE 15 kpc Pt	⋯	< 25	< 23
NW 5 kpc Ex	221±4	83±3	< 13
NW 5 kpc Pt	327±6	145±5	< 19
NW 10 kpc Ex	89±5	36±3	< 19
NW 10 kpc Pt	132±7	64±5	< 27
NW 15 kpc Ex	36±2	< 13	< 13
NW 15 kpc Pt	53±3	< 22	< 18

Note. — The measured line fluxes are given in 10^{-19} W m^{-2}.
[a] Integrated over the SH aperture (53 arcsec^2).
[b] Integrated over the LH aperture (248 arcsec^2).

factors provided in SPICE, and these two extreme limits bracket the true (unknown) distribution of gas in the slits. A comparison of the H_2 28 μm line fluxes for the two nod positions in both galaxies shows differences of <10%, suggesting the gas distribution is relatively smooth on the size scale of the nods (five and nine arcseconds, respectively, for SH and LH slits). Extended emission is also suggested by structure along the slit in individual images. We consider the distribution of the emission-line gas to be close to flat and extended, and apply the corresponding calibration, but also quote, for reference, the very unlikely values derived by applying the point source calibration, when interpreting the properties of the observed galaxies.

For the LH spectra of NGC 4565, we encountered a low-level "fringing" effect not seen in the spectra of NGC 5907. This effect would normally have been removed had we obtained dedicated "off" observations (not obtained during our Cycle-1 observations), and appears to be the result of incomplete "jail bar" removal in the pipeline (an effect in which parts of the detector array show a patterning, which in this case was brighter than usual). To remove this effect, we decided to use the observations taken at 15 kpc southeast (SE) of the nucleus of NGC 4565 as a reference, and subtracted this LH spectrum from all the others. This led to a significant improvement in the spectra. Nonetheless, such a procedure runs the risk that there may have been faint emission at that reference position which would be removed from all other LH points (this primarily affects the H_2 0–0 S(0) line which lies in the LH module). However, unlike the 15 kpc northwest (NW) point, which clearly shows 28 μm S(0) emission even before we performed the subtraction, the SE point appears devoid of emission as can be seen in Figure 4. We feel confident, therefore, that the use of the SE 15 kpc spectrum as a reference has not adversely affected our conclusions. Although faint emission might have been present in this reference spectrum, based on measurements of the raw spectrum of NGC 4565 at the 15 kpc SE position, we believe that an rms upper limit to such emission is 1.2×10^{-21} W m^{-2} Hz^{-1} at the posi-

tion of the 0–0 S(0) line, corresponding to less than 10% of the faintest H_2 emission detected at the 15 kpc NW point. In other words, the subtraction of the reference spectrum from the observations introduces a systematic error (not to be confused with a random error) which is estimated to be less than 10% of the faintest emission detected, a result that does not affect the conclusions of this paper. None of the SH spectra were affected by this instrumental effect.

Finally, we combined (by averaging) the spectra obtained at the two nod positions at each separate radial distance. The final spectra are shown in Figures 5 and 6.

3. RESULTS

The 0–0 S(0) and 0–0 S(1) transitions of H_2 were detected at the 5 and 10 kpc distances from the nucleus in both galaxies. H_2 was also detected at the northwest 15 kpc location in NGC 4565. On this side of the galaxy there is also substantially more H I emission (Rupen 1991). The 0–0 S(2) transition of H_2 was also detected in the Seyfert nucleus of NGC 4565. A variety of forbidden lines ([Ne II] 12.81 μm, [Ne III] 15.55 μm, [S III] 18.71/33.48 μm, and [Si II] 34.82 μm) were detected in most locations of both galaxies.

The continuum emission from the nucleus of NGC 4565 appears relatively flat, although it shows the broad PAH emission feature around 17 μm. Because the IRS apertures cover several hundred parsecs, most of this PAH emission is likely emitted by the disk of this galaxy. In addition to the forbidden lines detected elsewhere in this galaxy, [S IV] 10.51 μm, [Ne V] 14.32/24.31 μm, and [O IV] 25.89 μm were detected in the nucleus. The indicator lines of active galactic nuclei (AGNs), [Ne V] 14.32 μm and [Ne V] 24.31 μm (e.g., Armus et al. 2004), were both detected at a signal-to-noise ratio of ∼10.

3.1. *Line Fluxes*

We extracted line fluxes by fitting Gaussians to the lines using the SMART software package (Higdon et al. 2004). We fitted the broad aromatic features (indicated in Figures 5 and 6) with Lorentzian profiles (cf. the Lorentzian method used by Galliano et al. 2008). The extracted fluxes are given in Tables 1, 2, 3, 4, and 5, where "Pt" indicates point source calibrated spectra and "Ex" indicates fluxes corresponding to a flat, infinitely extended distribution, as explained in detail in Section 2.

The uncertainties were estimated by taking into account the quality of the profile fit. Generally high signal-to-noise ratios (> 10) were obtained for most of the lines except in the outer regions of the disks. Upper limits were estimated as $4 \times \sigma \times \delta\lambda$, where σ is the rms noise in the region of the expected line and $\delta\lambda$ is the width of an unresolved line at the corresponding wavelength (which corresponds essentially to the width of the bandpass for the high resolution modules, $\lambda/600$).

To assist in diagnosing the gas excitation conditions, we also estimated the flux densities in the IRAC 8 μm images of NGC 4565 and NGC 5907, under the areas covered by the IRS slits in our observations. We used the same IRAC 8 μm filter width as Roussel et al. (2007) to convert the flux densities from Jy into fluxes in W m^{-2},

Table 4
Forbidden line fluxes in NGC 5907.

Position	[NeII]12.81μm[a]	[NeIII]15.55μm[a]	[SIII]18.71μm[a]	[SIII]33.48μm[b]	[SiII]34.81μm[b]
SE 5 kpc Ex	187±5	33±2	70±4	386±21	553±9
SE 5 kpc Pt	284±7	55±4	127±7	613±33	906±14
SE 10 kpc Ex	48±2	21±3	30±2	197±14	201±7
SE 10 kpc Pt	72±3	35±5	54±4	312±22	329±11
SE 15 kpc Ex	< 12	< 13	< 13	< 21	< 31
SE 15 kpc Pt	< 18	< 22	< 24	< 34	< 51
NW 5 kpc Ex	168±8	31±5	50±2	379±12	481±4
NW 5 kpc Pt	254±12	52±8	90±4	602±19	789±6
NW 10 kpc Ex	28±2	8±0.4	13±2	115±10	146±4
NW 10 kpc Pt	43±3	14±0.6	24±3	182±16	239±7
NW 15 kpc Ex	< 14	< 7	< 18	< 22	< 32
NW 15 kpc Pt	< 21	< 12	< 33	< 35	< 53

Note. — The measured line fluxes are in 10^{-19} W m^{-2}.
[a] Integrated over the SH aperture (53 arcsec^2).
[b] Integrated over the LH aperture (248 arcsec^2).

Table 5
H$_2$ line fluxes in NGC 5907.

Position	0–0 S(0)[b]	0–0 S(1)[a]	0–0 S(2)[a]
SE 5 kpc Ex	180±7	92±5	< 16
SE 5 kpc Pt	267±10	162±8	< 24
SE 10 kpc Ex	51±2	18±2	< 12
SE 10 kpc Pt	75±3	32±3	< 18
SE 15 kpc Ex	< 17	< 9	< 9
SE 15 kpc Pt	< 25	< 16	< 14
NW 5 kpc Ex	188±3	104±3	< 13
NW 5 kpc Pt	278±4	182±6	< 20
NW 10 kpc Ex	51±3	15±2	< 15
NW 10 kpc Pt	76±4	27±3	< 22
NW 15 kpc Ex	< 18	< 13	< 16
NW 15 kpc Pt	< 26	< 23	< 24

Note. — The measured line fluxes are in 10^{-19} W m^{-2}.
[a] Integrated over the SH aperture (53 arcsec^2).
[b] Integrated over the LH aperture (248 arcsec^2).

but we have not attempted to subtract the stellar emission from the IRAC image as it is generally only a few per cent of the total emission at 8 μm.

3.2. *Ionized Gas Line and PAH Feature Ratios*

To investigate the gas excitation conditions we compared the strengths of various emission lines by forming line ratios. When comparing line ratios formed from lines taken with two different modules (LH and SH), we scaled the fluxes by a factor of 4.66, the ratio of the areas of the two module apertures. We also applied the extended source calibration correction to the line fluxes before taking the ratio to be consistent with this approach.

We show the line ratios in Figures 7 and 8. In NGC 4565 the [S III] 33.48 μm/[S III] 18.71 μm ratios are close to 1, typical for extranuclear regions seen in the SINGS sample of nearby galaxies (Dale et al. 2009), except at 10 kpc SE where the ratio drops below 0.4. This would imply a drop in the electron density by factors of a few hundreds (Dale et al. 2009). This ratio is slightly higher, between 1 and 2, in NGC 5907, covering very well the region in which most of the extranuclear areas studied by Dale et al. (2009) fall. The

[Si II] 34.81 μm/[S III] 33.48 μm ratio in NGC 4565 has a surprisingly low value of just above 1 at the nucleus, which is at the lower end of values seen in the nuclei of AGN galaxies in the sample of Dale et al. (2009).

The [Ne III] 15.55 μm/[Ne II] 12.81 μm ratio behaves as expected in both galaxies. It is higher in low-metallicity regions (towards larger radii in both galaxies), and lower towards the center in regions that are expected to have a higher metallicity. It achieves a high value in the nucleus of NGC 4565, consistent with what was seen by Dale et al. (2009) in the SINGS sample, presumably due to the higher excitation conditions near an AGN.

The H$_2$ S(0) to H$_2$ S(1) ratio hovers around 0.5 in both galaxies and is seen to increase towards the outer disk in both galaxies on both sides of the disk. This may primarily be an effect of the temperature, and it will be discussed in more detail in Section 3.3. We also show the H$_2$ S(0) to [S III] 33.48 μm ratio. [S III] 33.48 μm is mostly excited by star formation, and thus this ratio can be used as a rough indicator of the significance of star formation induced excitation of the H$_2$ molecule. We see that the ratio stays fairly constant at around 0.5 in both galaxies, but goes up at the 15 kpc NW point in NGC 4565. This is consistent with the ionization level of molecules dropping in the outermost disk, as discussed in Section 4.2 below. Figure 9 shows the ratios of the fluxes in the 11.3 and 7.7 μm PAH features versus the distance from the nucleus on the NW side of NGC 4565. The IRAC 8 μm fluxes measured in the IRAC image within the SH aperture and at the same spatial locations as the spectra were used as a proxy for the 7.7 μm PAH flux. The ratio is increasing towards 15 kpc NW, which most likely implies that the ISM is becoming less ionized towards the outer disk, as the 7.7 μm PAH feature consists of more ionized dust material than the 11.3 μm PAH feature (e.g., Allamandola, Hudgins, & Sandford 1999).

3.3. *Excitation Diagrams*

We constructed excitation diagrams (Figures 10 and 11) from the H$_2$ data in order to place constraints on the molecular gas properties. These diagrams plot the column density (N_u) of H$_2$ in the upper level of each transition, normalized by its statistical weight, versus the upper level energy E_u (e.g., Rigopoulou et al. 2002), which
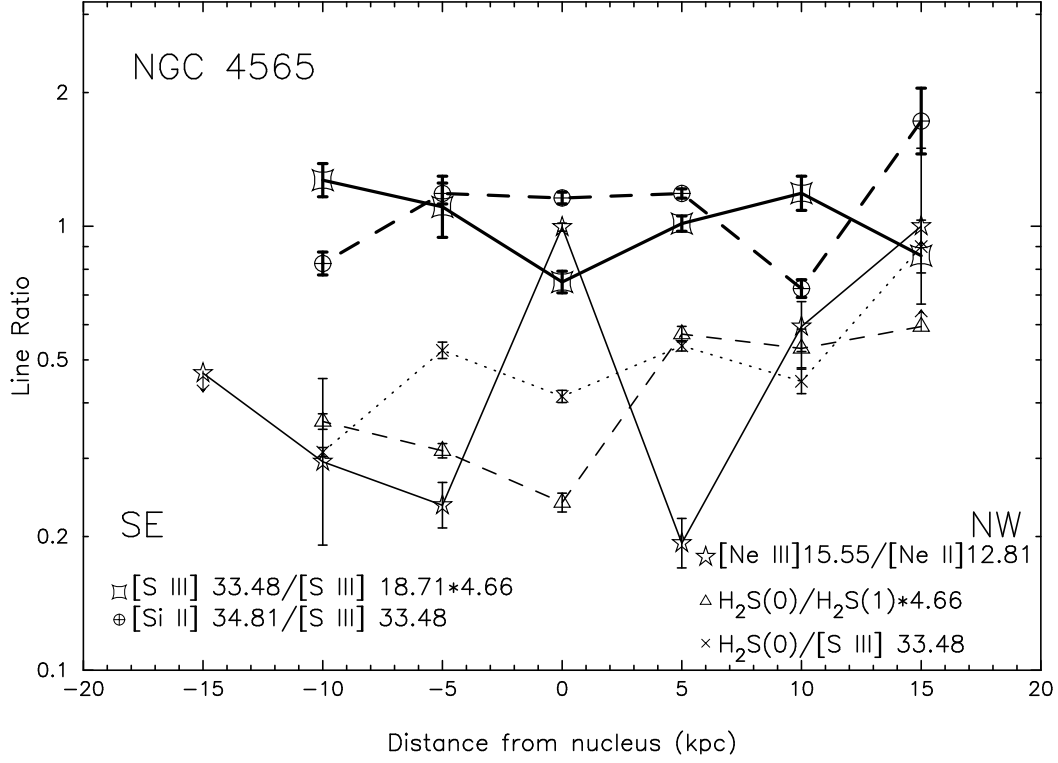
Figure 7. Line ratios in NGC 4565. The solid thin line is for [Ne III]/[Ne II], the dashed thin line is for H_2 S(0)/H_2 S(1), the dotted line is for H_2 S(0)/[S III] 33.48, the thick solid line is for [S III] 33.48/[S III] 18.71, and the dashed thick line is for [Si II] 34.81/[S III] 33.48.
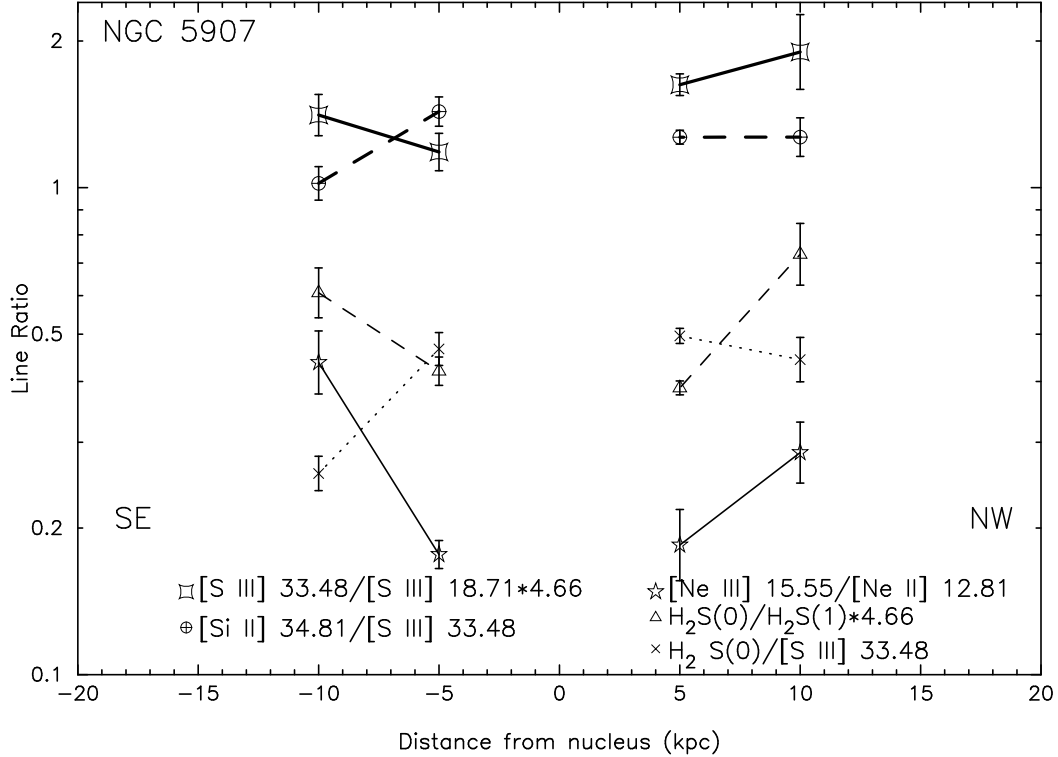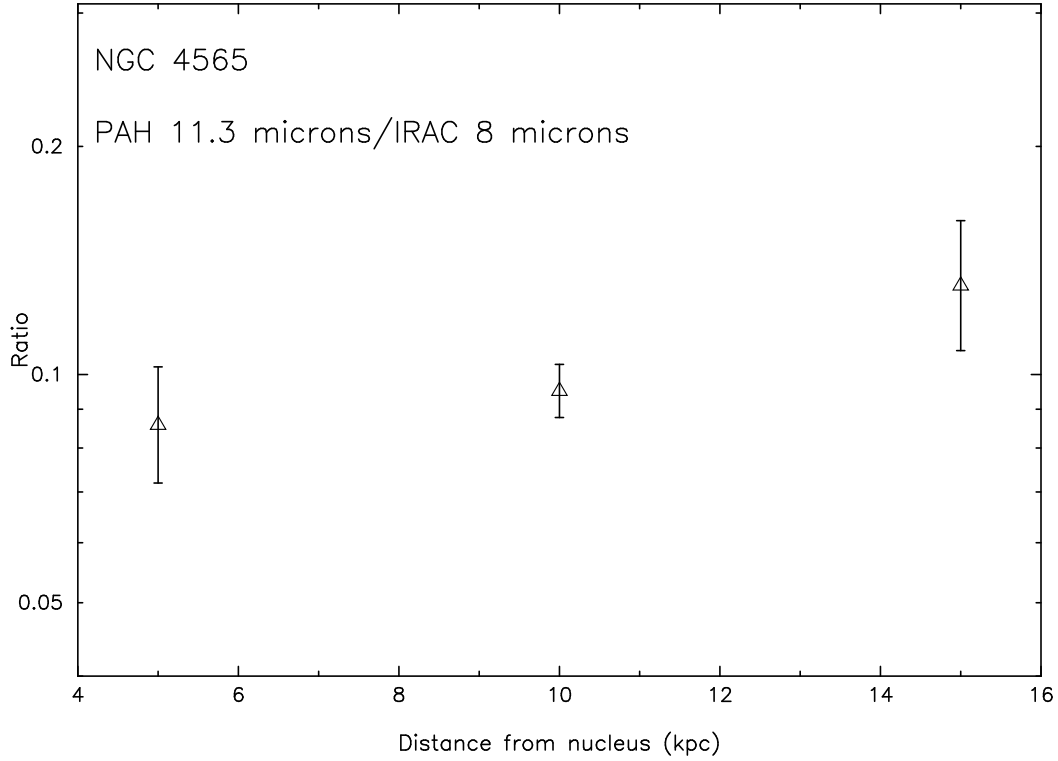

Figure 8. Line ratios in NGC 5907. The solid thin line is for [Ne III]/[Ne II], the dashed thin line is for H_2 S(0)/H_2 S(1), the dotted line is for H_2 S(0)/[S III] 33.48, the thick solid line is for [S III] 33.48/[S III] 18.71, and the dashed thick line is for [Si II] 34.81/[S III] 33.48.

Figure 9. Ratios of the fluxes in the 11.3 μm and 7.7 μm PAH features are plotted versus the distance from the nucleus (in kpc) on the northwestern side of NGC 4565. As explained in Section 3.2, the IRAC 8 μm flux is used as a proxy for the 7.7 μm PAH feature.

Table 6
Physical parameters derived from the excitation diagrams for NGC 4565

Position (kpc)	Temperature[a] (K)	Equilibrium o/p	N_{H_2} (10^{20} mol cm^{-2})	Σ_{H_2} (M$_\odot$ pc^{-2})
Nuc	$164 - (122)$	$2.6 - (2.0)$	$4.1 - (59)$	$6.6 - (95)$
SE 5	$149 - (112)$	$2.5 - (1.9)$	$4.8 - (74)$	$7.7 - (119)$
SE 10	$146 - (110)$	$2.4 - (1.8)$	$2.4 - (40)$	$3.8 - (64)$
NW 5	$135 - (106)$	$2.3 - (1.7)$	$7.5 - (113)$	$12. - (182)$
NW 10	$132 - (104)$	$2.3 - (1.7)$	$3.3 - (51)$	$5.2 - (82)$
NW 15	$<136 - (103)$	$2.3 - (1.6)$	$1.1 - (21)$	$1.8 - (34)$

[a] The values in parentheses are for the point source approximation.

Table 7
Physical parameters derived from the excitation diagrams for NGC 5907.

Position (kpc)	Temperature[a] (K)	Equilibrium o/p	N_{H_2} (10^{20} mol cm^{-2})	Σ_{H_2} (M$_\odot$ pc^{-2})
SE 5	$139 - (107)$	$2.4 - (1.8)$	$5.8 - (90)$	$9.3 - (145)$
SE 10	$129 - (101)$	$2.2 - (1.6)$	$2.0 - (32)$	$3.3 - (51)$
NW 5	$142 - (109)$	$2.4 - (1.8)$	$5.7 - (89)$	$9.2 - (144)$
NW 10	$124 - (100)$	$2.1 - (1.6)$	$2.3 - (33)$	$3.6 - (53)$

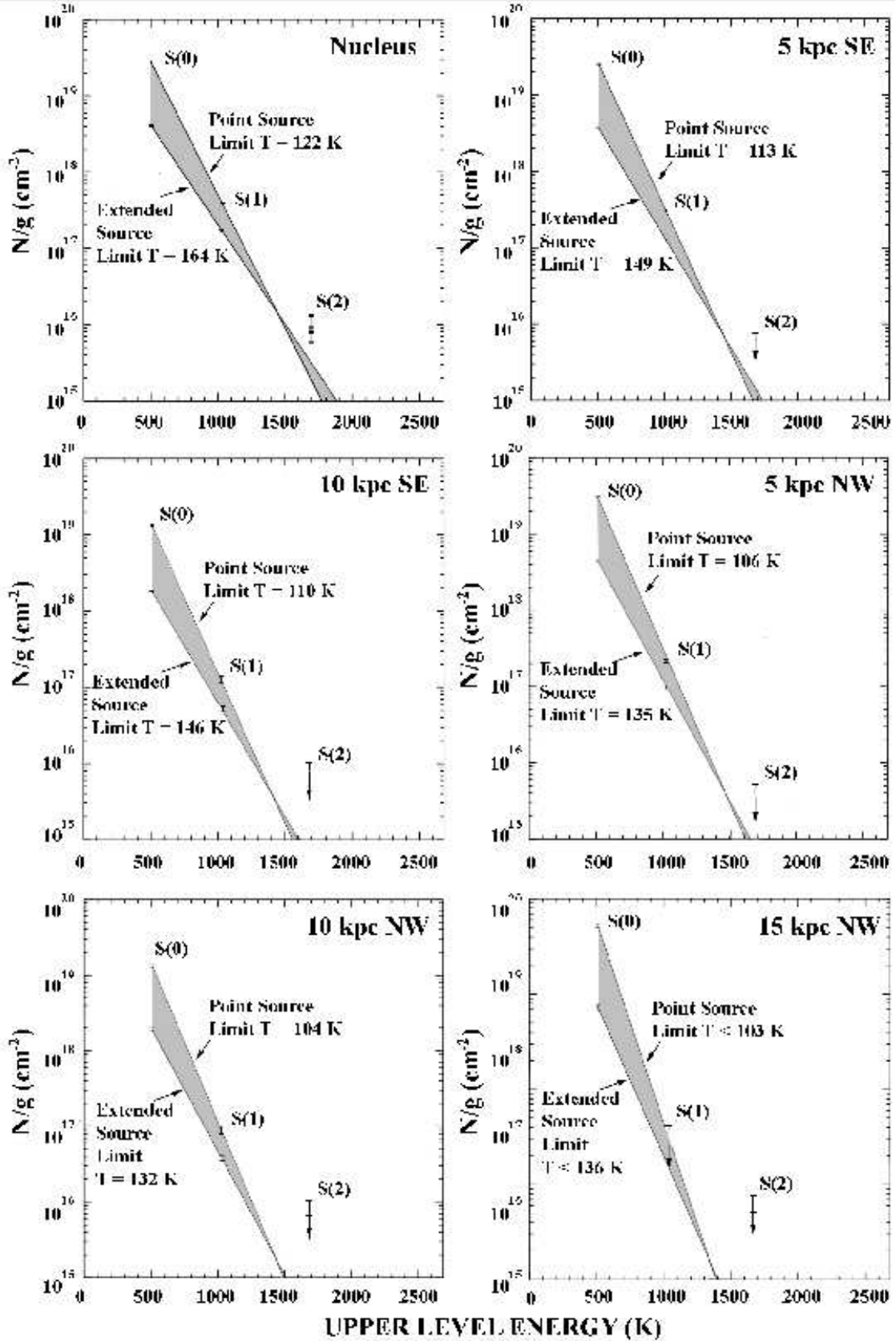[a] The values in parentheses are for the point source approximation.

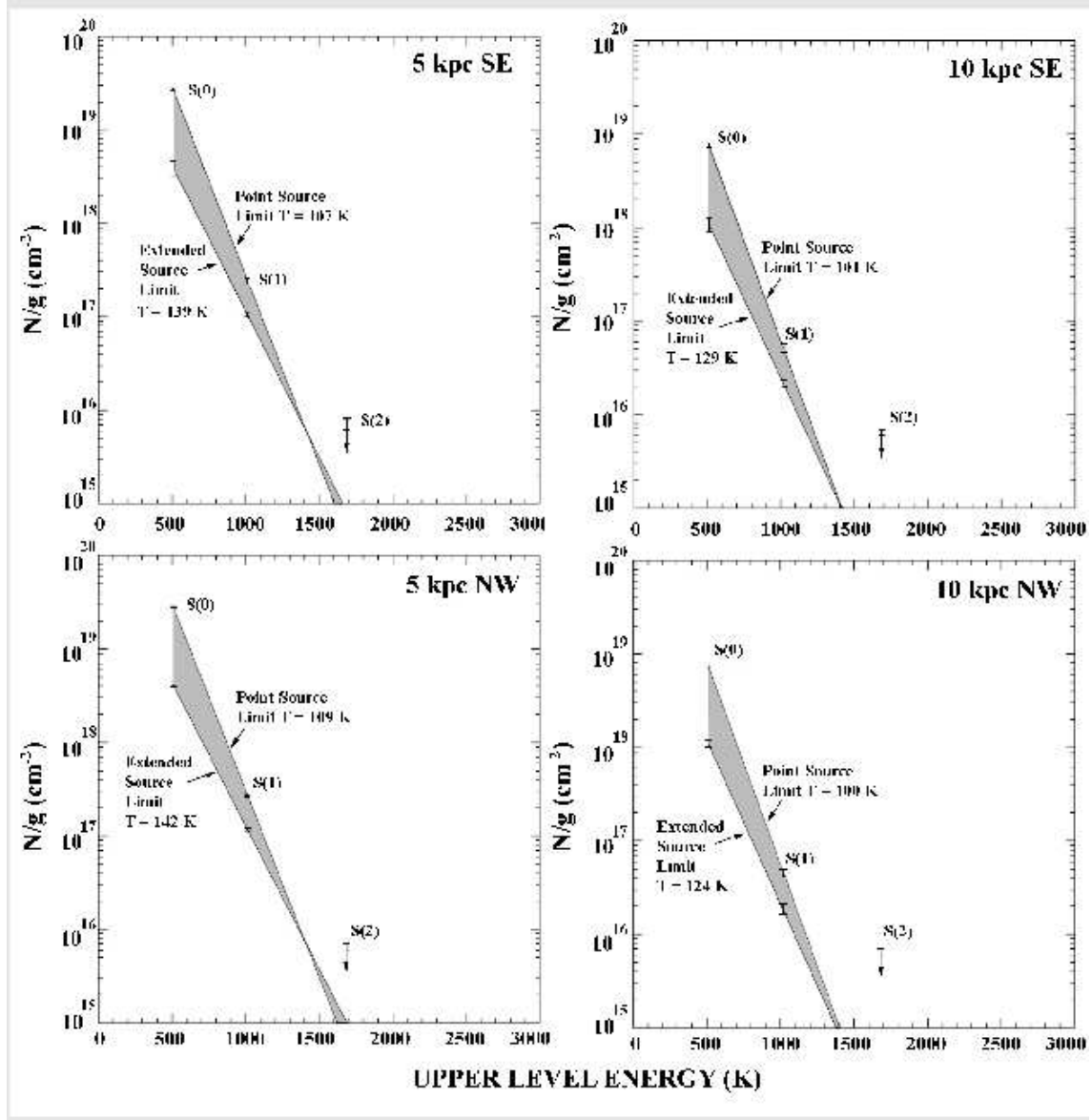**Figure 10.** Excitation diagrams for the disk positions of NGC 4565. The H$_2$ column density in the upper level of the transition normalized by its statistical weight (in cm^{-2}) is plotted versus the upper level energy (in K) for the S(0), S(1), and S(2) transitions at all locations except 15 kpc SE from the nucleus. Most S(2) data points are only upper limits. The solid lines indicate the best fits to the data points assuming a single-temperature component. The molecular hydrogen gas temperatures implied by the fits are shown. As discussed in Section 3.3, most likely there are multiple temperature components and the shown temperatures are very likely upper limits.

Figure 11. Excitation diagrams for NGC 5907. The H_2 column density in the upper level of the transition normalized by its statistical weight (cm^{-2}) is plotted versus the upper level energy (K) for the S(0), S(1), and S(2) transitions for the four inner locations. The S(2) data points are only upper limits. The solid lines indicate the best fits to the data points assuming a single-temperature component. The molecular hydrogen gas temperatures implied by the fits are shown.
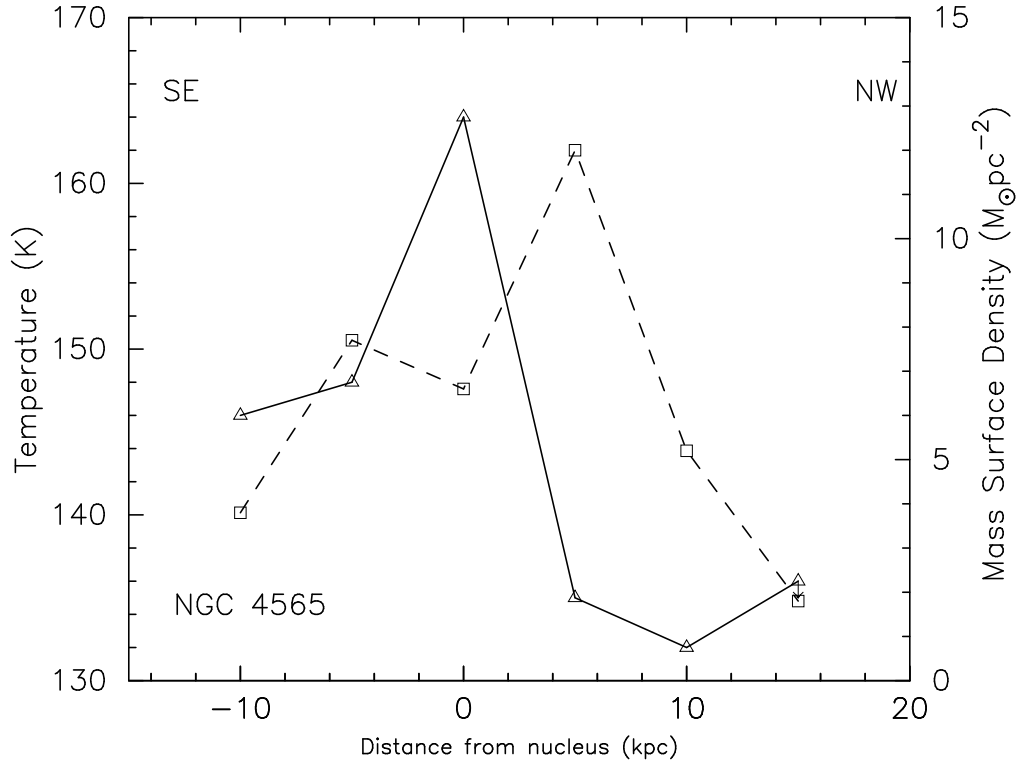
Figure 12. Temperature in K (solid line) and the mass surface density in $M_\odot$ pc^{-2} (dashed line) are plotted versus distance from the nucleus (in kpc) for NGC 4565. The estimates of temperature and mass surface density were derived from the H_2 S(0) and S(1) lines, and also the S(2) line in the nucleus. The temperature and mass surface density calculations were made with the assumption that the warm molecular H_2 gas is uniformly distributed across the slits (see Sections 2 and 3.3 for discussion on the flux distribution in the slits and the calibration differences between smooth, extended and point source fluxes).

we derived from the measured fluxes assuming local thermodynamic equilibrium for each position observed. Both extended and point source flux distributions are shown for the detected lines. The extended source results include a wavelength-dependent slit-loss correction which makes the extended flux calibration differ from the point source flux calibration typically by a factor of 1.5, and has a further geometrical correction of 4.66 for the different areas of the SH and LH slits. The grey area between the two limiting cases (point and extended) is the parameter space that most likely encompasses the actual case. However, we stress that the point source assumption is very unrealistic, as discussed in Section 2 and given the small slit aperture and the thickness of the disks. As we will see, this assumption also leads to unlikely low gas temperatures close to 100 K, and therefore high implied H_2 gas surface densities. For this reason we prefer to consider the extended source limit to be much closer to the actual situation, but the point source provides a useful (although unrealistic) boundary. The uncertainty in the H_2 properties is governed largely by this uncertainty in the slit loss corrections rather than the formal errors, which are quite small because the lines were all detected with quite high signal to noise ratios (SNR; they vary from 10 to 50 in most cases).

The solid lines indicate the best fits to the S(0), S(1), and S(2) data points assuming H_2 in thermal equilibrium with a single-temperature component (we will discuss the consequences of relaxing this assumption below). The fits also assume a thermal equilibrium ratio for the ortho-to-para species (O/P), as is reasonable if the density of the H_2 is above the critical density (which, for the low

J transitions, is typically $\sim$ 100 mol cm^{-3}), a condition probably satisfied in most cases. For temperatures less than $\sim$ 300 K, this leads to O/P ratios $<$ 3. For example, at T = 115–120 K, O/P = 2 for thermal equilibrium. However, it is far from clear that thermal equilibrium is appropriate in all cases. For example, if the excitation mechanism were a shock, then the passage of the shock could leave the H_2 molecules in a state where they do not have enough time to equilibrate. This is another source of uncertainty. For example, if O/P was 3 instead of 2 (a case where the gas has not had time to come into thermal equilibrium), then this would change the calculated temperature from T = 120 K to 113 K with a corresponding increase in the total H_2 mass surface density. This uncertainty in the O/P ratio is comparable with the uncertainty in the clumpiness in the H_2 distribution which leads to the broad range of possible temperatures as shown in Figures 10 and 11.

The single-temperature fits to these data are shown in each panel of the figures. Outside the nucleus only an upper limit is available for the S(2) line. Therefore, fitting more than one thermal component is not statistically justifiable – the fits are the formal solutions. We note that the assumption that the source of H_2 is a point source always yields very low H_2 temperatures, bordering on becoming physically unreasonable. Thus we believe that the warmer temperatures implied by the extended source calibration are more physically reasonable for the case of these edge-on galaxies. One exception is the nucleus of NGC 4565, where a point-source assumption may be reasonable, as it contains a Seyfert nucleus.
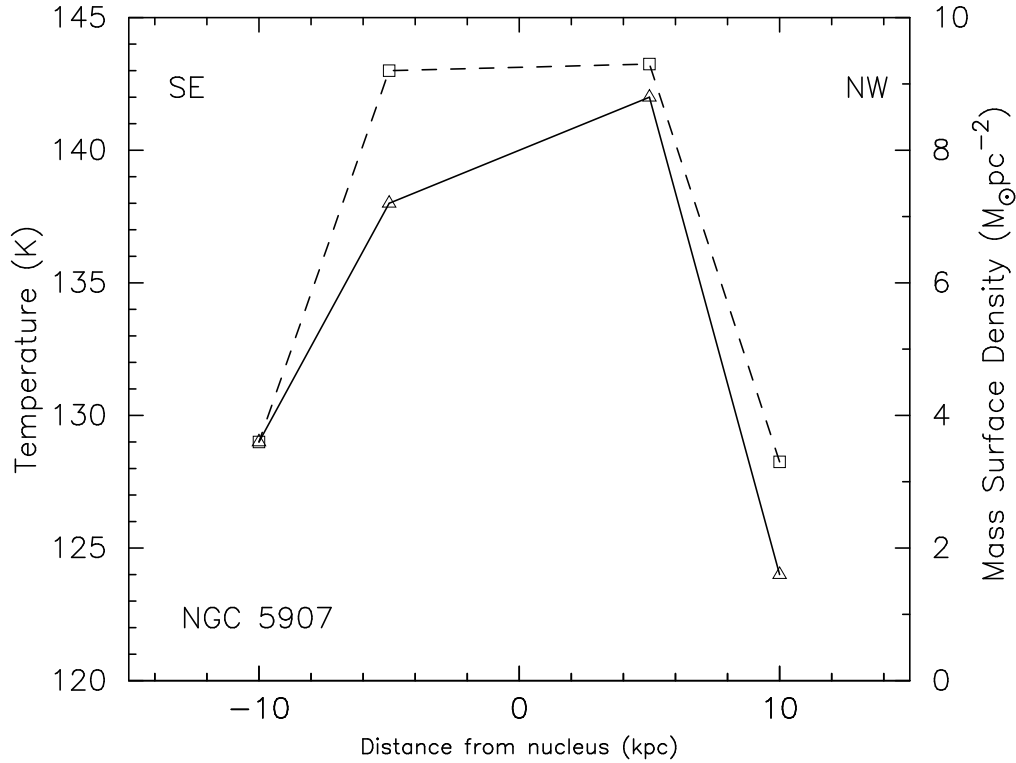
Based on these assumptions, Tables 6 and 7 summa-

Figure 13. Temperature in K (solid line) and the mass surface density in $M_\odot$ pc^{-2} (dashed line) are plotted versus distance from the nucleus (in kpc) for NGC 5907. The estimates of temperature and mass surface density were derived from the H$_2$ S(0) and S(1) lines. The temperature and mass surface density calculations were made with the assumption that the warm molecular H$_2$ gas is uniformly distributed across the slits (see Section 2 and 3.3 for discussion on the flux distribution in the slits and the calibration differences between smooth, extended and point source fluxes).

rize the derived H$_2$ physical parameters for NGC 4565 and NGC 5907, respectively: temperature (K), equilibrium ortho/para ratio, column density of H$_2$ (mol cm^{-2}), and the mass surface density of H$_2$ ($M_\odot$ pc^{-2}). The temperatures and mass surface densities for NGC 4565 and NGC 5907 are also shown in Figures 12 and 13. The gas is colder in the outer disk where the mass surface density is also lower, creating the apparent impression of a correlation between temperature and mass surface density. The derived (extended source) mass surface densities are more than 100 times smaller than those found in NGC 891 by Valentijn & van der Werf (1999). See Section 4.3 for more discussion about the implication of the implied warm H$_2$ mass surface densities.

If one adopts the extended source assumption, and excludes the nucleus of NGC 4565 which is significantly warmer, there is no obvious change in the fitted temperature with radius within the uncertainty from $r = 5$ kpc to $r = 10$ kpc on both sides of this galaxy (T = 146–149 K on the southeastern side and T = 132–134 K on the northwestern side). Even at $r = 15$ kpc on the northwestern side, the upper limit to the S(1) flux provides a temperature limit which is at least consistent with a flat temperature distribution. The situation is different in NGC 5907, where the outermost 10 kpc points seem more than 10 K cooler than those measured at 5 kpc. For this galaxy the radial temperature profile is also symmetric, unlike that in NGC 4565.

In the previous discussion we have made an assumption that a single-temperature model is reasonable. This is clearly not the case for the nucleus of NGC 4565, where

the 0–0 S(2) line was detected. The first panel of Figure 10 shows that the single-temperature fits do not pass through the S(2) point. Indeed, in general, extragalactic sources almost always show a range of allowable temperatures and often a multiple-component fit is required. One consequence of fitting a multiple-temperature model is that the warmer component softens the slope of the fit in the excitation diagram. This means that the lower temperature component becomes even cooler, once a warm component is subtracted. To illustrate this we have fitted a two-component model to the nucleus of NGC 4565 and derived the following temperatures and column densities. Instead of a single (in this case point-like) nuclear source with T = 122±4 K and a column density N_{H_2} of 5.9×10^{21} mol cm^{-2}, we obtain T(1) = 115±3 K, $N(1)_{H_2} = 7.4 \times 10^{21}$ mol cm^{-2}, and T(2) = 450–550 K, $N(2)_{H_2} = 3$–4×10^{18} mol cm^{-2}. The warmer component is less constrained because the error bar on the S(2) line is larger than that of the S(0) and S(1) lines. Note that the effect in this case of relaxing the single-temperature model is to increase the cold component column density by 25%. The warmer component adds a negligible amount to the final column density.

It is very likely that the nucleus of NGC 4565 is different from the disk because it contains a Seyfert component which may contribute additional heating to the H$_2$ emission. This is reflected in the generally higher single-temperature fits shown in Figure 10. It may seem odd that the two-component fit gives a temperature for the cold component in the nuclear pointing that is colder than elsewhere in the disk. However, the thermodynam-

ics of the H_2 molecule is likely to be very complex, involving a multi-phase medium with unknown heating and cooling conditions. It is also possible that the density distribution of the clouds near the nucleus is very different from elsewhere in the disk, and there may be more very dense cold clouds near the nucleus. With the spatial resolution afforded by the IRS, we cannot resolve this question. Furthermore, magnetohydrodynamic shocks may be driven into a clumpy medium near the nucleus, which will lead to a range of temperatures. It should also be noted that it is impossible to estimate what the separate contributions of the disk and the nucleus are to the observed line fluxes in the nuclear pointings.

Thus, depending on the strength of a second or third component, the temperature of the coolest component is always lowered relative to a single-temperature fit-case. Because we used only single-temperature fits, it is possible that we underestimated the total H_2 column density if warmer components were present, because a cooler H_2 temperature implies a larger total H_2 column density. Since we have, in general, no information about a warmer component, we cannot do more than fit a single-temperature component and accept a degree of uncertainty in the final H_2 column densities and masses.

4. DISCUSSION

4.1. Nucleus of NGC 4565

The line fluxes measured in the Seyfert nucleus of NGC 4565 are listed in Table 2. The continuum appears relatively flat, although it shows a signature of the broad PAH emission feature around 17 μm. Since the apertures are relatively large (covering several hundreds of pc), a lot of this PAH emission is likely to come from the disk of NGC 4565. The 11.3 μm and 12.9 μm PAH features are also strong, but weaker than in the spectra taken at 5 kpc from the nucleus. The detected emission lines come from H_2, O, Ne, S, and Si. The AGN indicator lines of [Ne V] 14.32 μm and [Ne V] 24.31 μm (e.g., Armus et al. 2004) are both detected at S/N $\sim$ 10. The H_2 S(0)/H_2 S(1) ratio reaches its minimum at the nuclear position (see Figure 7), implying the highest gas temperatures, as can also be seen in Figure 10. The [Ne III] 15.55 μm/[Ne II] 12.81 μm ratio reaches a peak in the nucleus. The value of $\sim$ 1 for this ratio indicates a moderate nuclear starburst (Verma et al. 2002). It is also consistent with the classification of NGC 4565 as a Sy1.9 galaxy (Deo et al. 2007).

4.2. Gas, Dust, and PAH Excitation

In both galaxies, NGC 4565 and NGC 5907, we see that the emission line intensities and the derived mass surface densities of H_2 emission (as well as the intensity of the forbidden lines) decrease with increasing radius, while the temperature decreases only slightly. Also, the 20-cm radio continuum, for NGC 4565 shown in Figure 14 (Sukumar & Allen 1991), decreases strongly towards the 15 kpc radius (which in NGC 4565 is actually outside the detected radio continuum emission on the NW side).

We calculated the ratio of the H_2 luminosity surface density over the total infrared (TIR) emission luminosity surface density (Figure 15). TIR was calculated as in equation (9) of Bendo et al. (2008) over the LH slit area, measuring surface brightness values in the 8, 24,
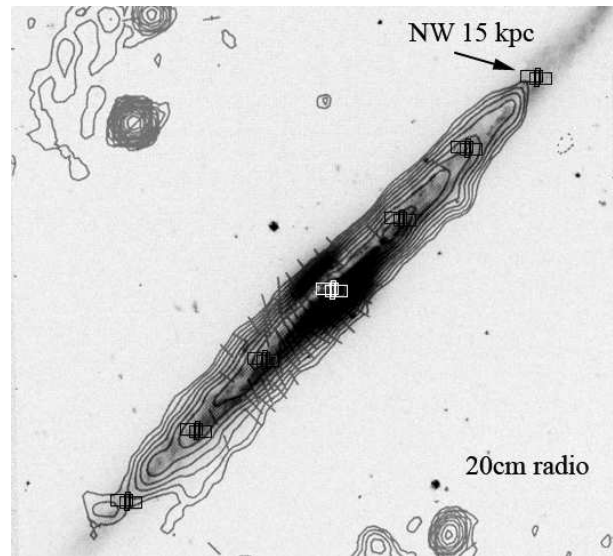

Figure 14. 20-cm radio continuum emission in NGC 4565 from Sukumar & Allen (1991), shown on top of an optical image.

70, and 160 μm Spitzer IRAC and MIPS maps that were all smoothed to the resolution of the 160 μm map, at the positions of the observed IRS slits. This ratio is relatively constant with the radius at about 0.2%–0.4%. This value is somewhat higher than the 0.05%–0.1% typically seen in the SINGS sample, but since we could not match the resolution and aperture of the broad-band images, from which TIR was estimated, to the single slit observations taken in the staring mode, such a bias is expected.

When plotting the H_2 emission power over the IRAC 8 μm power (Figure 16) we see that the points in NGC 4565 and NGC 5907 lie generally above the star formation region points in Roussel et al. (2007). Specifically, we see an increase in the ratio towards the outer 15 kpc NW point in NGC 4565. We also see no change in the H_2 S(0)/11.3 μm PAH ratio (Figure 17) on the northwestern side of the disk of NGC 4565, but we see an increase in the 11.3 μm/7.7 μm PAH feature ratio (Figure 9) from 10 kpc to 15 kpc. One explanation is that the PAHs become more neutral in the lower UV excitation environment of the outer disk at 15 kpc NW in NGC 4565. The possible change in PAH excitation from ionized to neutral changes the relative strengths of the 11.3 μm with respect to the 7.7 μm PAHs because the 11.3 μm PAH feature becomes more dominant as the PAHs become more neutral. This might naturally explain why the 15 kpc NW point in Figure 15 stands out. It is not due to the H_2 emission becoming relatively stronger at 15 kpc, but due to the 7.7 μm PAH feature becoming weaker.

We also measured the 24 μm flux densities in the areas covered by the IRS slits in NGC 4565, and noticed that the 24 μm flux density decreases with radius. Since the 24 μm emission is a relatively good proxy of the star formation intensity (e.g., Calzetti et al. 2007), this implies that the UV flux intensity is decreasing with radius, therefore producing a more neutral ISM at larger radii, consistent with our results derived from the PAH flux ratio.
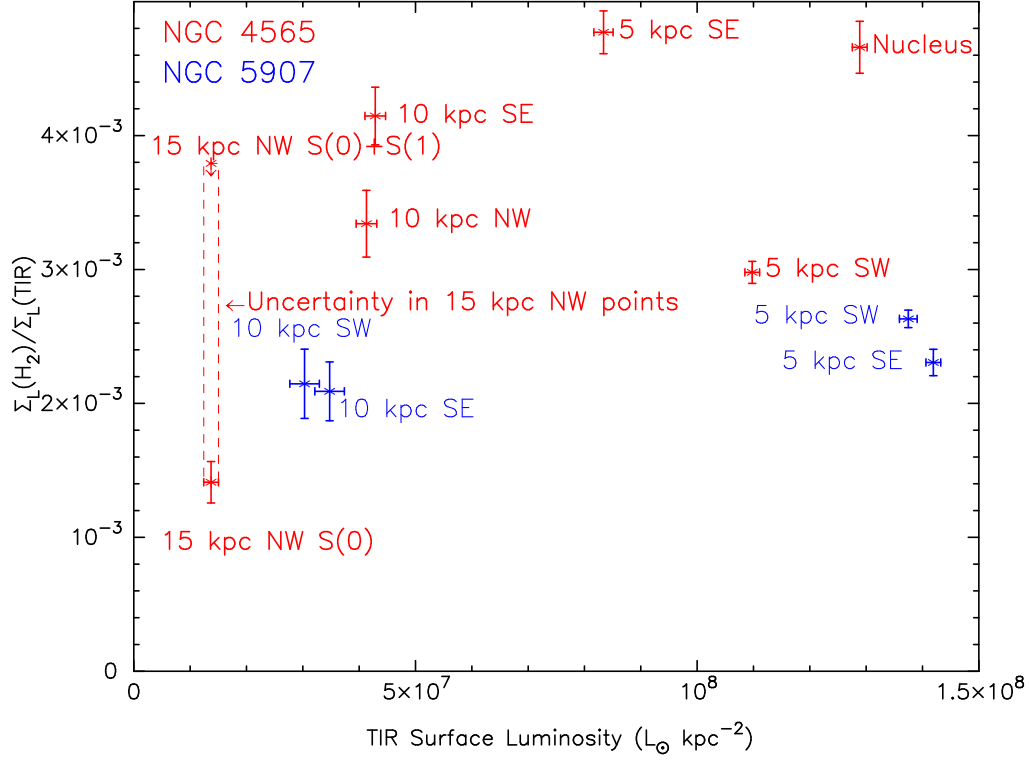
Figure 15. Ratios of the H_2 and total infrared (TIR) luminosity surface densities in NGC 4565 and in NGC 5907. Details on the calculation of TIR are given in Section 4.2.
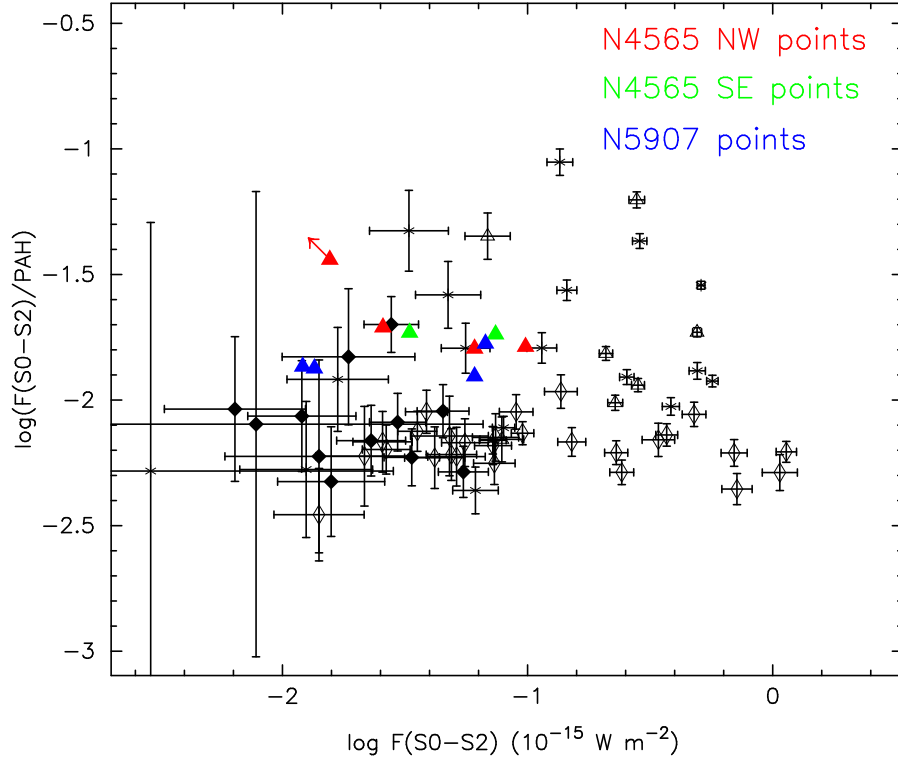

Figure 16. Logarithm of the ratios of the H_2 emission to the 8 μm emission for NGC 4565 and NGC 5907. NGC 4565 is shown in red and green colors and NGC 5907 is shown in blue colors. As in Roussel et al. (2007), the open diamonds are for star forming regions, filled diamonds for dwarf galaxies, stars for nuclear regions containing a LINER nucleus, and triangles for nuclear regions containing a Seyfert galaxy.

4.3. *Warm Molecular Gas Contribution to Dark Mass in the Disks of NGC 4565 and NGC 5907*

Hoekstra, van Albada & Sancisi (2001) have shown that there is an apparently strong coupling between the surface densities of neutral hydrogen and dark matter in spiral galaxies, with a significant and pronounced peak in $\Sigma_{DM}/\Sigma_{HI} \sim 9$. To see whether this holds in NGC 5907, we used the multicomponent dynamical model of NGC 5907 by Barnaby & Thronson (1994). For ease of calculation we approximated the dark matter distribution by a singular isothermal sphere. At a radial distance of 10 kpc from the nucleus we calculate a Σ_{DM} = 188 $M_{\odot}$ pc^{-2}. $\Sigma_{HI} \sim 17.4$ $M_{\odot}$ pc^{-2} (Sofue 1994) and the ratio of the two is 10.8. Including the warm H_2 gas only reduces the dark matter to gas ratio to 9. Thus NGC 5907 appears to follow the relationship found by Hoekstra et al. (2001). At a radial distance of 15 kpc from the nucleus the warm H_2 is undetected. Assuming, as suggested by the data, an extended, smooth emission distribution, $\Sigma_{H_2} \leq 3$ $M_{\odot}$ pc^{-2}. Using our approximation to the Barnaby–Thronson model, $\Sigma_{DM}/\Sigma_{H_2} \geq 42$. At 15 kpc, $\Sigma_{HI} = 10.3$ $M_{\odot}$ pc^{-2} and $\Sigma_{DM}/\Sigma_{HI} = 12.2$. It is therefore clear that the mass of the ISM in NGC 5907, including the mass of the warm molecular gas, is too small by more than an order of magnitude to account for the requisite dark matter.

Unfortunately there is no model of the mass distribution and dynamics of NGC 4565 similar to that of Barnaby & Thronson (1994) for NGC 5907. The neutral atomic hydrogen properties were studied by Rupen (1991), and the cold molecular gas properties by Sofue & Nakai (1994) while visible light surface photometry of NGC 4565 was performed by van der Kruit & Searle (1981). We assumed that the stars and the ISM are confined to a thin disk and the dark halo can be described, again, by a singular isothermal sphere. The rotation curve is given by Sofue (1996, 1997). van der Kruit & Searle (1981) showed that the optical disk is truncated at a radius of 24.9 kpc, comparable to where Rupen (1991) sees a warp. Using a B-band luminosity of the old disk of 1.4×10^{10} $L_{\odot}$ and a median value of 7.5 (corrected for Hubble constant $H_0 = 75$ km s^{-1} Mpc^{-1}) for the mass to luminosity ratio of Sab–Sb galaxies from Roberts & Haynes (1994), the mass of the luminous stellar disk is 10.5×10^{10} $M_{\odot}$. This may be an overestimate as some fraction of the mass quoted by Roberts & Haynes (1994) is dark. The total mass of the neutral atomic hydrogen is 5.96×10^9 $M_{\odot}$ (Rupen 1991) and that of the cold molecular hydrogen 2.4×10^9 $M_{\odot}$ (Sofue & Nakai 1994). We assumed that the ISM and the stars are confined to a thin disk and all components are truncated at 25 kpc. Lequeux (1983) suggests that the velocity at the truncation radius is

$$V^2 = \frac{GM}{0.6R} \qquad (1)$$

where R is 25 kpc for NGC 4565 and M is the total mass. Beyond $R=25$ kpc the velocity is assumed to decline in a Keplerian fashion. At a radial distance of 35 kpc, the observed circular velocity of the galaxy is about 214 km s^{-1} (Sofue 1997). From the mass and velocity components of our model we find that the halo

contributes a velocity of 150 km s^{-1} to the system. We reflect these values back to a radius of 15 kpc at which we observed the most distant emission from warm H_2, and we recalculate the mass surface densities. Assuming a singular isothermal sphere for the dark matter, the mass surface density of dark matter is 86 $M_{\odot}$ pc^{-2}, the ratio of the mass surface densities of dark matter and warm H_2 (with the much likelier smoothly distributed extended source emission calibration) is $\geq 86/1.8 = 48$, and that of dark matter to all of the ISM components (neutral atomic hydrogen, warm molecular hydrogen, and cold molecular hydrogen) is ≥ 15.

From our analysis it is clear that the mass surface densities of the warm molecular gas cannot produce the observed rotation velocities at large radii in NGC 4565 and NGC 5907. The "missing mass" in these two galaxies cannot be accounted for by warm H_2 gas.

4.4. *Source of Excitation of H_2 in the Outer Disk of NGC 4565*

The molecular gas at the 15 kpc NW point in the outer disk of NGC 4565, as probed by the H_2 rotational lines, has roughly the same temperature and the same ratio of the H_2 to far-IR power as in the inner disk. However, the star formation rate at the 15 kpc NW point, traced by the mid-IR emission, has substantially decreased, compared to the inner disk. In other words, although the intensity of the exciting radiation field has been reduced (as seen also in the change in the ratio of the ionized to neutral PAH molecules and in a reduction in the TIR intensity when comparing the 10 kpc NW and 15 kpc NW points), the molecular gas is heated to a similar temperature throughout the disk. Therefore, something other than star formation may be heating the gas at the 15 kpc NW point.

Cosmic ray (CR) heating of the H_2 does not appear viable at the 15 kpc NW point because we see a dramatic decrease in the strength of the synchrotron radio continuum emission, which is a tracer of cosmic rays accelerated in the magnetic field of the galaxy, between the 10 and 15 kpc NW points, as shown in Figure 14. The 15 kpc NW point lies outside the detectable signal in the radio continuum maps of Sukumar & Allen (1991). The upper limit of the 20-cm radio continuum (150 μJy/beam; 3σ) at the 15 kpc NW point suggests a difference of a factor of > 64 in the 20-cm radio continuum flux density between the 10 and 15 kpc points. This change is not reflected in the decrease in the H_2 line luminosity which is only a factor of 7.

However, despite the lack of detected radio continuum at the 15 kpc NW point, we cannot completely rule out CR excitation. If we assume an equipartition of energy between CRs in the disk and the magnetic energy density, the upper limit to the radio continuum flux density corresponds to an upper limit for the equipartition magnetic field strength of $B_{min} \leq 1$ μG, following the assumptions discussed in Govoni & Feretti (2004). This corresponds to a magnetic energy density (and a comparable CR energy density) of $\sim 9.6 \times 10^{-14}$ ergs cm^{-3}. For a canonical synchrotron lifetime in the mid-plane of 10^7 yrs, the CRs could potentially provide $L_{cr} \leq 4.7 \times 10^{30}$ W/kpc^2 of power if such a population of CRs existed below the detection limit of the radio continuum observations. In-

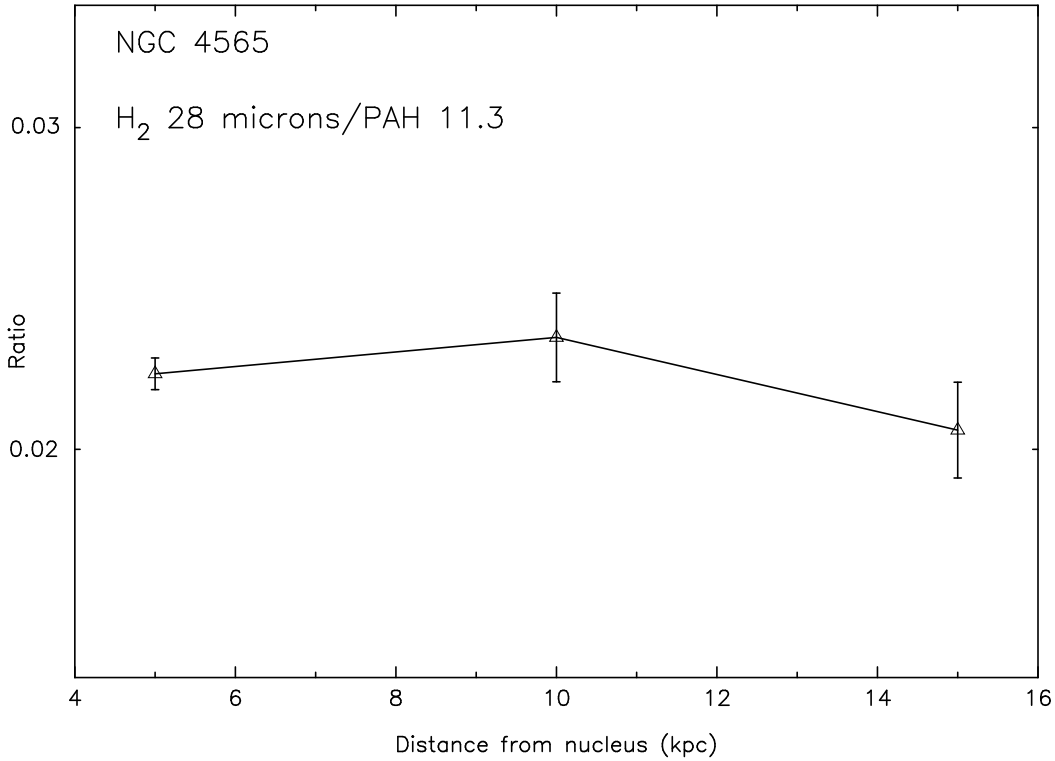**Figure 17.** Ratios of the fluxes of H$_2$ S(0) 28 μm and the 11.3 μm PAH feature are plotted versus the distance from the nucleus (in kpc) on the northwestern side of NGC 4565.

terestingly, this is only a factor of two lower than the H$_2$ line luminosity in the S(0) line at 15 kpc NW (7 $\times$ 10^{30} W/kpc^2), and therefore CR heating, although unlikely (it would require very rapid deposition timescales of much less than 10^7 yrs and high heating efficiency), cannot be completely ruled out.

We note that the equivalent $B_{\rm min}$ and $L_{\rm cr}$ for the 10 kpc NW point in NGC 4565 are 3.3 μG and 5.0 $\times$ 10^{-13} ergs cm^{-3}, respectively[1], and the ratio of $L_{\rm cr}/L({\rm H}_2) \sim 0.5$ at that point. This suggests that within the radio continuum emitting disk of NGC 4565, trapped cosmic rays can, in principle, provide energy to heat the H$_2$ in the disk (again high heating efficiency would be needed). In those same regions, star formation, through PDR heating, provides a more likely channel for heating the H$_2$ gas (see Roussel et al. 2007).

The feasibility of cosmic ray heating at $r = 15$ kpc can also be estimated using an independent ionization argument (Guillard 2009). If we assume that the cosmic rays heat the gas through partial ionization of the H$_2$ to H$_3{}^+$, then the rate of ionization through cosmic ray heating must balance the rate of cooling of the H$_2$ per molecule. For a column density $N_{\rm H_2} \sim 1.1 \times 10^{20}$ mol cm^{-2} and the observed luminosity in the S(0) line, we estimate the H$_2$ cooling per molecule to be 6.7 $\times$ 10^{-33} W mol^{-1}. Yusef–Zadeh, Wardle, & Roy (2007) estimate the CR heating rate per molecule to be 8 $\times$ 10^{-18} $\zeta_{\rm H}$ W, where $\zeta_{\rm H}$ is the H$_2$ ionization rate. Under these assumptions, for CR heating to balance the H$_2$ cooling would require an ionization rate of $\sim 10^{-15}$ s^{-1}. This value is comparable to that measured in the Galactic Center

(see Oka et al. 2005), but is unlikely to be realized in the outer disk of NGC 4565. This again suggests that CR excitation is an unlikely source of heating for the S(0) line at $r = 15$ kpc unless conditions there are very unusual.

The two remaining options for H$_2$ excitation in the outer disk are heating within extended PDR regions, or shock heating. We have already shown that the ratio of the H$_2$ power to the far-IR emission power is consistent with PDR heating (in comparison with the models of Draine et al. 2007), but it is not clear if this process works in the outer disk. Indeed, it is very likely (and observations with the *Herschel Space Observatory* will help to resolve this issue) that a large component of the TIR flux we see in the outer disk of NGC 4565 comes from cirrus clouds heated by the general radiation field of the outer disk, and not from young stars. Thus one is left with the puzzling result that the H$_2$ excitation remains constant to within a factor of two in the outer disk which does not contain a high concentration of young stars. Widely distributed PDR regions around a smoothly distributed set of faint young stars may be responsible for the excitation, but this cannot be demonstrated with our observations.

Another possible way of heating the H$_2$ is by shocks, perhaps through a recent passage of a disturbance through the outer disk of NGC 4565. A recent model of how H$_2$ can be excited in a powerful shock propagating through a multi-phase medium in Stephan's Quintet has been presented by Guillard et al. (2009). However, this model was tuned to the specific problem of how to generate large amounts of power in the H$_2$ lines in a 1000 km sec^{-1} shock moving through a clumpy medium. To explain the emission in the outer regions of NGC 4565 via shocks would require considerably less energy input,

---

[1] Here we assume that the depth of the radio continuum emitting region is 10 kpc at $r = 10$ kpc and 5 kpc at $r = 15$ kpc.

but there is no obvious source of energy to drive the shocks. Curiously, recent *Spitzer* observations of a high-latitude cirrus cloud within the Galaxy (Ingalls et al. 2010) have revealed unusually strong H_2 emission from regions that are clearly not associated with PDRs. Shock heating is one possible explanation. These observations suggest that the excitation of H_2 in galaxy disks is not yet well understood.

5. CONCLUSIONS

We have examined the excitation of gas, dust, and PAHs and the physical conditions of the ISM in two nearby normal edge-on disk galaxies, NGC 4565 and NGC 5907, out to 15 kpc from the nucleus of each galaxy. Our most important conclusions can be summarized as follows.

1. We have detected the rotational 17 μm S(0) and 28 μm S(1) H_2 line transitions at 5 and 10 kpc, and most interestingly, the S(0) H_2 line at 15 kpc NW from the nucleus of NGC 4565.

2. We have discovered that in these two edge-on galaxies, NGC 4565 and NGC 5907, the warm molecular gas temperature (although uncertain) and the ratio of the H_2 line luminosity surface density to the total infrared luminosity surface density are rather flat with radius. However, the active star formation rate, as measured by, e.g., the 24 μm emission, falls rapidly with radius. This result is potentially inconsistent with excitation of the H_2 emission by photodissociation regions in the outer disks of these galaxies.

3. Alternatives to the H_2 excitation in the outer disk are cosmic ray heating and shocks. Based on the midplane radio continuum emission intensities, excitation by cosmic rays and photodissociation regions are both viable in the inner disk. However, in the outer disk the non-detection of radio continuum implies that cosmic rays are less important there. Therefore, extended photodissociation regions or shocks can excite the emission at the outermost disk, as seen in NGC 4565 at the 15 kpc NW point.

4. We see an increase of the 11.3 μm/7.7 μm PAH feature strength ratio (where we used the IRAC 8 μm band to be a proxy of the 7.7 μm emission) at the 15 kpc NW position in NGC 4565. We also see that the summed H_2 line intensity over the 8 μm emission intensity ratio increases at the same position. Our interpretation is that the H_2 S(0) 28 μm emission at the 15 kpc NW position may still be excited by (weaker) emission from photodissociation regions, coming from a more neutral medium at this large distance from the nucleus, as the strength of the 7.7 μm PAH feature, which traces more highly ionized dust, decreases with respect to the strength of the 11.3 μm PAH feature, which traces more neutral dust.

5. The observations strongly suggest that the warm molecular gas is smoothly distributed. Assuming such an extended distribution, the detected mass surface densities of warm molecular hydrogen are very low at large radii in both galaxies. It is very unlikely that this component of the ISM contributes at any significant level to the "missing mass" in the outer regions of these two edge-on disk galaxies.

6. The Seyfert 1.9 nucleus in NGC 4565 revealed [Ne V] 14.32 μm, [Ne V] 24.31 μm, [S IV] 10.51 μm, and [O IV] 25.89 μm lines, as well as the 12.28 μm H_2 S(2) line. The higher excitation forbidden lines are expected to be seen in Seyfert nuclei.

Facilities: Spitzer (IRAC, IRS, MIPS)

REFERENCES

Allamandola, L. J., Hudgins, D. M., & Sandford, S. A. 1999, ApJ, 511, L115

Alton, P.B., Xilouris, E. M., Misiriotis, A., Dasyra, K. M., & Dumke, M. 2004, A&A, 425, 109

Appleton, P. N., et al. 2006, ApJ, 639, L51

Armus, L., et al. 2004, ApJS, 154, 178

Armus, L., et al. 2006, ApJ, 640, 204

Barnaby, D., & Thronson, H. A., Jr. 1994, AJ, 107, 1717

Bendo, G., et al. 2008, MNRAS, 389, 629

Brunner, G., et al. 2008, ApJ, 675, 316

Calzetti, D., et al. 2007, ApJ, 666, 870

Cluver, M., et al. 2010, ApJ, 710, 248

Dale, D. A., et al. 2009, ApJ, 693, 1821

Deo, R. P., Crenshaw, D. M., Kraemer, S. B., Dietrich, M., Elitzur, M., Teplitz, H., Turner, T. J. 2007, ApJ, 671, 124

Draine, B. T., et al. 2007, ApJ, 663, 866

Galliano, F., Madden, S. C., Tielens, A. G. G. M., Peeters, E., & Jones, A. P. 2008, ApJ, 679, 310

García–Burillo, S., Guélin, M., & Neininger, N. 1997, A&A, 319, 450

Govoni, F., & Feretti, L. 2004, IJMPD, 13, 1549

Guillard, P. 2009, Ph.D. thesis, Univ. Paris-Sud

Guillard, P., Boulanger, F., Pineau des Forêts, G., & Appleton, P. N. 2009, A&A, 502, 515

Higdon, S. J. U., et al. 2004, PASP, 116, 975

Hoekstra, H., van Albada, T. S., & Sancisi, R. 2001, MNRAS, 323, 453

Houck, J., et al. 2004, ApJS, 154, 18

Ingalls, J. G., Bania, T. M., Draine, B. T., Boulanger, F.,
    Falgarone, E., & Hily-Blant, P. 2010, in ASP Conf. Ser.,
    Reionization to Exoplanets: Spitzer's Growing Legacy, ed. P.
    Ogle, in press
Lequeux, J. 1983, A&A, 125, 394
Neininger, N., Guelin, M., Garcia-Burillo, S., Zylka, R., &
    Wielebinski, R. 1996, A&A, 310, 725
Ogle, P., Antonucci, R., Appleton, P. N., Whysong, D. 2007, ApJ,
    668, 699
Ogle, P., Boulanger, F., Antonucci, R., Appleton, P. N.., Evans,
    D.A, Leipski, C., & Nesvadba, N. 2010, ApJ, submitted
Oka, T., Geballe, T. R., Goto, M., Usuda, T., & McCall, B. J.
    2005, ApJ, 632, 882
Rachford, B. L., et al. 2009, ApJS, 180, 125
Rigopoulou, D., et al. 1996, A&A, 315, L125
Rigopoulou, D., Kunze, D., Lutz, D., Genzel, R., Moorwood, A.
    F. M. 2002, A&A, 389, 374
Roberts, M. S., & Haynes, M. P. 1994, ARA&A, 32, 115
Roussel, H., et al. 2007, ApJ, 669, 959
Rupen, M. P. 1991, AJ, 102, 48

Sancisi, R. 1976, A&A, 53, 159
Shang, Z., et al. 1998, ApJ, 504, L23
Shaw, G., Ferland, G. J., Henney, W. J., Stancil, P. C., Abel, N.
    P., Pellegrini, E. W., Baldwin, J. A., & van Hoof, P. A. M.
    2009, ApJ, 701, 677
Snow, T. P., et al. 2000, ApJ, 538, L65
Sofue, Y. 1994, PASJ, 46, 173
Sofue, Y. 1996, ApJ, 458, 120
Sofue, Y. 1997, PASJ, 49, 17
Sofue, Y., & Nakai, N. 1994a, PASJ, 46, 147
Sukumar, S., & Allen, R. J. 1991, ApJ, 382, 100
Valentijn, E. A., & van der Werf, P. P. 1999, ApJ, 522, L29
Valentijn, E. A., van der Werf, P. P., de Graauw, T., & de Jong,
    T. 1996, A&A, 315, L145
van der Kruit, P.C., & Searle, L. 1981, A&A, 95, 105
Verma, A., Lutz, D., Strum, E., Sternberg, A., Genzel, R., Vacca,
    W. 2002, A&A, 403, 829
Werner, M. W., et al. 2004, ApJS, 154, 1
Yusef–Zadeh, F., Wardle, M., & Roy, S. 2007, ApJ, 665, L123